

Toward precision Fermi-liquid theory in two dimensions

Silas R. Beane¹, Gianluca Bertaini², Roland C. Farrell¹, and William R. Marshall¹

¹*Department of Physics, University of Washington, Seattle, Washington 98195, USA*

²*Istituto Nazionale di Ricerca Metrologica, Strada delle Cacce 91, I-10135 Torino, Italy*



(Received 27 December 2022; accepted 10 March 2023; published 13 April 2023)

The ultracold and weakly coupled Fermi gas in two spatial dimensions is studied in an effective field theory framework. It has long been observed that universal corrections to the energy density to two orders in the interaction strength do not agree with Monte Carlo simulations in the weak-coupling regime. Here, universal corrections to three orders in the interaction strength are obtained, and are shown to provide agreement between theory and simulation. Special consideration is given to the scale ambiguity associated with the nontrivial renormalization of the singular contact interactions. The isotropic superfluid gap is obtained to next-to-leading order, and nonuniversal contributions to the energy density due to effective range effects, p -wave interactions, and three-body forces are computed. Results are compared with precise Monte Carlo simulations of the energy density and the contact in the weakly coupled attractive and repulsive Fermi-liquid regimes. In addition, the known all-orders sum of ladder and ring diagrams is compared with Monte Carlo simulations at weak coupling and beyond.

DOI: [10.1103/PhysRevA.107.043314](https://doi.org/10.1103/PhysRevA.107.043314)

I. INTRODUCTION

Dramatic improvements in the experimental control of atomic systems have led to intense theoretical interest in the quantum mechanics of interacting atomic gases. In particular, the ability to tune interaction strengths using Feshbach resonances, and to continuously vary the number of spatial dimensions using anisotropic harmonic traps and optical lattices, is allowing for precision experimental tests of a vast and quickly developing theoretical framework. This has attracted physicists from many areas of research who are interested in the few- and many-body quantum mechanics of nonrelativistic constituents. Simultaneous progress in numerical simulation [1], coupled with increased access to high-performance computing, has been occurring in parallel with the experimental developments. This rich interplay among theory, experiment, and computation has led to what might be considered a golden age of atomic physics.

An increasingly valuable tool for atomic systems that enables model-independent descriptions of both bosonic and fermionic gases is effective field theory (EFT).¹ Historically in atomic physics, studies of gases with constituents interacting via finite-range potentials have utilized specific solvable models of the two-body interaction, like the hard-sphere potential. While these models capture the essential physics of finite-range potentials, EFT allows for the study of interacting gases in a manner that is independent of any specific potential. The resulting interaction, viewed in coordinate space, is a sequence of potentials consisting of delta functions and their derivatives, which are highly singular near the origin. However, the divergent nature of the interaction is straightforward to control using regularization and renor-

malization, and can be exploited by considering the renormalization-group (RG) flow of coupling constants. The main utility of the EFT framework is that it provides a clear strategy for the systematic improvement of the quantum-mechanical descriptions of fundamental properties of atomic gases at weak coupling. These improvements include, for example, pairing and finite-temperature effects, nonuniversal modifications to the equation of state, nonisotropic interactions, many-body forces and shape-parameter corrections, as well as dimensional-crossover scenarios. The EFT treatment of weakly coupled Fermi gases in three spatial dimensions has been developed in Refs. [5–17]. In this paper, these EFT techniques will be adapted and applied to the study of weakly coupled Fermi gases in two dimensions.²

Experimentally, the Fermi gas in a quasi-two-dimensional (2D) environment is accessible via highly anisotropic harmonic traps that effectively confine a spatial dimension. This requires *inter alia* a special theoretical treatment which accounts for the continuous compactification of the third dimension. However, recent numerical simulations using Monte Carlo (MC) techniques allow a precise, direct computation of the zero-temperature equation of state in two spatial dimensions from weak coupling all the way to the BCS–Bose-Einstein-condensate (BEC) crossover region [19–24]. It has been observed that the energy density obtained from these simulations is in tension with theoretical calculations at weak coupling, which have been carried out to second order in the universal coupling [25–27]. In this paper, the calculation of the energy density is carried out to third order in the universal coupling and is found to resolve the tension between theory and simulation.

¹For general reviews, see Refs. [2,3], and for an atomic-physics oriented review, see Ref. [4].

²For a comprehensive review of the Fermi gas in two dimensions, see Ref. [18].

Consider a gas of fermions of mass M in two or three spatial dimensions with two-body interactions that are of finite range R and typical energy scale U . The dimensionless parameters $k_F R$ and MU/k_F^2 , where k_F is the Fermi momentum, are the knobs which determine the strength of the interaction. Without fine tuning one expects that the ground state of the Fermi gas will be dominated by the leading s -wave two-body interactions, which are governed by the two-dimensional (three-dimensional) scattering lengths, a_2 (a_3). Unlike the case with a_3 , whose sign in the weakly interacting regime is indicative of whether the interaction is attractive or repulsive, a_2 is intrinsically positive. The relevant dimensionless parameter is $k_F a_2$ ($k_F a_3$) and weak coupling is therefore achieved either at low density (dilute limit), or with weak two-body interactions. Due to the presence of a Fermi surface, an arbitrarily weak attractive interaction leads to the formation of Cooper pairs and qualitatively changes the properties of the gas. At weak coupling, the gas is in the BCS phase characterized by large interparticle spacing k_F^{-1} and exhibits superfluidity or superconductivity. As the coupling increases, there is a transition to the BEC phase of tightly bound pairs, and it becomes natural to view the gas as a system of weakly repulsive bosonic dimers. Here dimensionality provides a drastic difference [18]. Whereas in three dimensions, attraction must be strong enough to sustain a bound state, in two dimensions there is a bound state for an arbitrarily weak interaction. This implies that in two dimensions the entire BCS-BEC crossover may be traversed by varying the density with an arbitrary attractive interaction, i.e., there are no new singularities introduced due to the formation of a bound state.

Many of the interesting and distinguishing features of the two-dimensional gas arise from the manner in which quantum effects break the scale invariance of the classical Hamiltonian and give rise to the effective coupling constant $-1/\ln(k_F a_2)$. This paper will be concerned with the weak-coupling limits: $|\ln(k_F a_2)| \gg 1$. With repulsive interactions the gas is a Fermi liquid with the energy density a straightforward perturbative expansion in the coupling. With attractive interactions the gas is a paired superfluid, but may be viewed as a Fermi liquid as long as the energy due to pairing is small as compared to the leading perturbative correction to the free Fermi gas. The various scale hierarchies relevant for a complete and systematic description of the weak-coupling regime may be precisely quantified in the EFT.

Beyond mean-field corrections to the energy of the weakly coupled Fermi gas in two dimensions with repulsive interactions were first considered in Refs. [25–27]. The attractive Fermi gas and the superfluid gap were treated in Refs. [28,29]. The goal of this paper is to consider the next order in the weak-coupling expansion, and to compare the results with MC simulations. It is important to stress that the subleading corrections that we compute have previously been found in two distinct studies whose aim was to perform resummations of classes of Feynman³ diagrams to all orders in the coupling [16,17]. A secondary goal of this paper is to obtain the leading nonuniversal effects, due to effective-range corrections,

p -wave interactions, and three-body forces, although it is not clear whether these latter two effects can be meaningfully compared with experiment or simulation at the present time. Indeed, the motivation for computing these effects is to inspire MC simulations which include more intricate few-body forces and enable a meaningful comparison with theory.

This paper is organized as follows. Section II introduces the effective Lagrangian density which encodes the interactions that are the basis of the necessary EFT technology, and considers the free-space power-counting scheme. In Sec. III, a general partial-wave expansion of the two-body scattering amplitude is given. With the assumption of finite-range forces, effective-range expansions of the s - and p -wave scattering amplitudes are defined. Finally, the scattering amplitudes are reproduced in the EFT using dimensional regularization (DR). The modifications of the free-space EFT technology to the treatment of interactions in medium are considered in Sec. IV. This section adapts the main results of Refs. [7,12] to the case of two spatial dimensions. In particular, the renormalized thermodynamic potential is obtained, and the superfluid gap is recovered using dimensional regularization. The Fermi-liquid expansion is treated to three orders in the expansion parameter in Sec. V. Nonuniversal corrections to the energy density are considered in Sec. VI. In Sec. VII, the final expression of the energy density is given at an arbitrary renormalization scale, and the contact is defined and obtained from the energy density. In Sec. VIII, resummation schemes which treat ladder [16] and ring [17] diagrams to all orders in the interaction strength are reviewed. Comparison of theoretical predictions of the weak-coupling regime with MC simulations is given in Sec. IX. Section X is a summary and conclusion.

II. EFFECTIVE FIELD THEORY TECHNOLOGY

A. Effective Lagrangian

Here it is assumed that the underlying interaction experienced by the fermionic atoms is of finite range, say R . Then, with a characteristic momentum scale represented by k , at momentum scales $k \leq R^{-1}$, the interaction takes the form of a sequence of contact interactions. The theory of contact interactions is described by an effective Lagrangian which consists of local operators constructed from the nonrelativistic fermion field ψ , which generally possesses g components.⁴ The local Lagrangian density is constrained to be Galilean and time-reversal invariant and can be expressed in the form

$$\begin{aligned} \mathcal{L} = & \psi^\dagger \left[i\partial_t + \frac{\vec{\nabla}^2}{2M} \right] \psi - \frac{C_0}{2} (\psi^\dagger \psi)^2 \\ & + \frac{C_2}{16} [(\psi \psi)^\dagger (\psi \nabla^2 \psi) + \text{H.c.}] + \frac{C'_2}{8} (\psi \nabla_i \psi)^\dagger (\psi \nabla_i \psi) \\ & - \frac{C'_4}{64} [(\psi \nabla_i \psi)^\dagger (\psi \nabla^2 \nabla_i \psi) + \text{H.c.}] - \frac{D_0}{6} (\psi^\dagger \psi)^3 \\ & + \dots, \end{aligned} \quad (1)$$

³Here all diagrams, both in free space and in a medium, are referred to as Feynman diagrams.

⁴Note that the three-dimensional relationship between degeneracy and spin, $g = 2s + 1$, holds when two dimensions is reached as a limiting case via dimensional reduction.

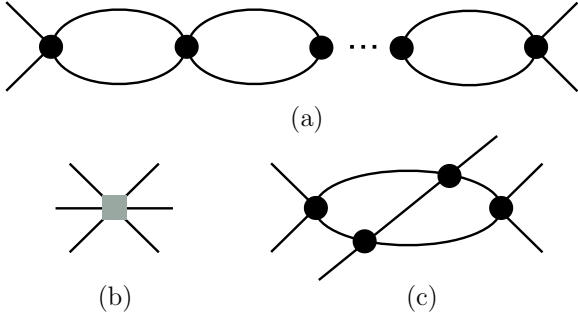


FIG. 1. (a) Two-body diagram with L loops. Three-body diagrams at tree level (b) and at two-loop level (c) (fish slash). The black circle (gray square) corresponds to an insertion of the C_0 (D_0) operator.

where $\nabla = \overleftarrow{\nabla} - \overrightarrow{\nabla}$ is the Galilean invariant derivative and H.c. symbolizes the Hermitian conjugate. Throughout the paper, $\hbar = 1$, and the fermion mass, M , is left explicit. The Lagrangian takes the same form in any spacetime dimension d , with the dimensions of the fermion field and of the operator coefficients given by $[\psi] = (d-1)/2$, $[C_{2n}^{(l)}] = 2-d-2n$, and $[D_{2n}] = 3-2d-2n$.

In two spatial dimensions ($d = 2 + 1$), the Lagrangian with only the C_0 interaction is scale invariant.⁵ This is most easily seen by rescaling the field and spatial coordinates by $\psi \rightarrow M^{1/2}\psi$ and $\mathbf{x} \rightarrow M^{-1/2}\mathbf{x}$, which removes all dimensionful parameters from the Hamiltonian obtained from Eq. (1). The resulting theory has a marginal contact interaction whose strength is proportional to the dimensionless coupling MC_0 . This symmetry does not survive quantization and is broken by the regularization of the singular C_0 interaction which necessarily introduces a scale into the theory. This constitutes a fundamental difference between the many-body physics of two and three dimensions.

B. Free-space counting scheme

By exploiting topological properties, it is found that a free-space Feynman diagram with L loops or E external lines and V_{2i}^n n -body vertices with $2i$ derivatives scales as $(kR)^\chi$, where

$$\begin{aligned} \chi &= (d-1)L + 2 + \sum_{n=2}^{\infty} \sum_{i=0}^{\infty} (2i-2)V_{2i}^n \\ &= d + 1 - \frac{1}{2}(d-1)E \\ &\quad + \sum_{n=2}^{\infty} \sum_{i=0}^{\infty} [2i + (d-1)n - d - 1]V_{2i}^n. \end{aligned} \quad (2)$$

The EFT has predictive power in three dimensions because at every order in kR there are a finite number of diagrams that contribute. In two dimensions there is a subtlety due to the scale invariance of the universal interaction (i.e., the effect of the C_0 operator), as noted above. In order to distinguish

two dimensions from three, it is instructive to power count the generic interactions illustrated in Fig. 1. The two-body diagram with L loops and $L+1$ insertions of C_0 , Fig. 1(a), has $\chi = L(d-3)$. Therefore, in three dimensions, there is a loop expansion⁶ with each loop bringing one additional power of kR . By contrast, in two dimensions, the two-body diagram with L loops has $\chi = 0$, a consequence of scale invariance, and an indication that universal interactions appear in a perturbative expansion in MC_0 . A further illustrative example is the leading three-particle interactions. The three-body diagram with an insertion of D_0 , Fig. 1(b), has $\chi = 0$ for all d . A leading three-body diagram with four C_0 insertions, Fig. 1(c), has $\chi = 2(d-4)$. Therefore, in three dimensions these three-body effects appear at the same order in the momentum expansion, as is necessary given that the two-loop diagram has a logarithmic divergence, which must be renormalized by the D_0 operator [34]. By contrast, in two spatial dimensions, these universal three-body diagrams require no new counterterms beyond C_0 , and indeed they appear at lower order in the power counting, indicating that three-body forces are enhanced in two dimensions.

III. TWO BODIES IN FREE SPACE

A. Partial-wave expansion

Consider two-body scattering, with incoming momenta labeled \mathbf{k}_1 and \mathbf{k}_2 and outgoing momenta labeled \mathbf{k}'_1 and \mathbf{k}'_2 . In the center-of-mass frame, $\mathbf{k} \equiv \mathbf{k}_1 = -\mathbf{k}_2$, $\mathbf{k}' \equiv \mathbf{k}'_1 = -\mathbf{k}'_2$, and $k \equiv |\mathbf{k}| = |\mathbf{k}'|$. In two dimensions, angular momentum is specified by counting the number of windings around the unit circle, including both clockwise and anticlockwise orientations. The unitary scattering amplitude can be expanded in partial waves as [35–37]

$$T(k, \phi) = \sum_{\ell=0}^{\infty} T_{\ell}(k, \phi) = \frac{4}{M} \sum_{\ell=0}^{\infty} \frac{\epsilon_{\ell} \cos(\ell\phi)}{\cot \delta_{\ell}(k) - i}, \quad (3)$$

where ϕ is the scattering angle, δ_{ℓ} is the phase shift, $\epsilon_0 = 1$ and $\epsilon_{\ell} = 2$ for $\ell > 0$, and the normalization has been chosen to match the Feynman diagram expansion.

The $\ell = 0$ (s -wave) scattering amplitude is then

$$T_0(k) = \frac{4}{M} \frac{1}{\cot \delta_0(k) - i}. \quad (4)$$

The effective range expansion takes the conventional form

$$\cot \delta_0(k) = \frac{1}{\pi} \ln(k^2 a_2^2) + \sigma_2 k^2 + O(k^4), \quad (5)$$

where a_2 is the scattering length⁷ and $\sqrt{|\sigma_2|}$ is the effective range. This form of the expansion appears odd from the EFT

⁶This assumes that the C_0 operator is of natural size. Near unitarity, each C_0 insertion brings an infrared enhancement of k^{-1} , leading to all loops counting equally and a consequent breakdown of perturbation theory [31–33].

⁷Another common convention for the definition of the scattering length coincides with the diameter a_{2D} in the case of the hard-disk potential, corresponding to $a_{2D} = 2a_2 \exp(-\gamma)$, where γ is the Euler-Mascheroni constant.

⁵In fact, this theory is also invariant under nonrelativistic conformal transformations (see Ref. [30]).

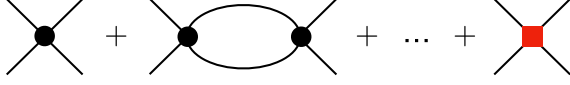


FIG. 2. Diagrams contributing to isotropic scattering. The black circle (red square) corresponds to an insertion of the C_0 (C_2) operator.

perspective since the leading effect at low k is nonanalytic in k . As will be seen below, this purely quantum-mechanical effect occurs because of strong infrared effects in two dimensions.

The $\ell = 1$ (p -wave) scattering amplitude is

$$T_1(k, \phi) = \mathbf{k} \cdot \mathbf{k}' \frac{8}{M} \frac{1}{k^2 \cot \delta_1(k) - ik^2}, \quad (6)$$

and the p -wave effective range expansion can be written as

$$k^2 \cot \delta_1(k) = -\frac{1}{\sigma_p} + \frac{1}{\pi} k^2 \ln(k^2 a_p^2) + O(k^4), \quad (7)$$

where σ_p is a scattering volume (units of area), and a_p is a length scale that characterizes higher-order effects in the momentum expansion. For $\sigma_p k^2 \ll 1$, the scattering amplitude can be expanded in perturbation theory to give

$$T_1(k, \phi) = -\sigma_p \mathbf{k} \cdot \mathbf{k}' \frac{8}{M} \left\{ 1 + \frac{1}{\pi} \sigma_p k^2 [\ln(k^2 a_p^2) - i\pi] + O[(\sigma_p k^2)^2] \right\}. \quad (8)$$

In the next subsection, these scattering amplitudes will be recovered in the EFT.

B. Scattering in the EFT: s wave

Consider s -wave scattering in the EFT described by the effective Lagrangian of Eq. (1).⁸ The sum of the Feynman diagrams shown in Fig. 2 is

$$T_0(k) = -C_0 - C_0^2 I_0(k) + \dots - C_2 k^2, \quad (9)$$

where

$$I_0(k) = M \left(\frac{\mu}{2} \right)^\epsilon \int \frac{d^{d-1} \mathbf{q}}{(2\pi)^{d-1}} \frac{1}{k^2 - q^2 + i\delta}, \quad (10)$$

and μ is the DR scale, and $\epsilon \equiv 3 - d$.⁹ As perturbative physics can always be treated nonperturbatively, it is convenient to neglect the C_2 contribution, and sum the bubble chain to all orders, giving

$$T_0(k) = -\frac{C_0}{1 - I_0(k)C_0}. \quad (11)$$

A useful integral is

$$\begin{aligned} I_n(k) &= M \left(\frac{\mu}{2} \right)^\epsilon \int \frac{d^{d-1} \mathbf{q}}{(2\pi)^{d-1}} q^{2n} \left(\frac{1}{k^2 - q^2 + i\delta} \right) \\ &= k^{2n} \frac{M}{4\pi} \left[\ln \left(-\frac{k^2}{\mu^2} \right) + \gamma - \ln \pi - \frac{2}{\epsilon} \right] \\ &= k^{2n} I_0(k), \end{aligned} \quad (12)$$

where n is a non-negative integer and the logarithmic divergence has been captured by the $1/\epsilon$ pole.

Using Eqs. (11) and (12) gives

$$T_0^{-1}(k) = -\frac{1}{C_0} + \frac{M}{4\pi} \left[\ln \left(-\frac{k^2}{\mu^2} \right) + \gamma - \ln \pi - \frac{2}{\epsilon} \right]. \quad (13)$$

Defining the renormalized EFT coefficient $C_0(\mu)$ with \overline{MS} results in

$$-\frac{1}{C_0} \equiv -\frac{1}{C_0(\mu)} - \frac{M}{4\pi} \left[\gamma - \ln \pi - \frac{2}{\epsilon} \right]. \quad (14)$$

This exact renormalization condition then gives the physical scattering amplitude:

$$T_0^{-1}(k) = -\frac{1}{C_0(\mu)} + \frac{M}{4\pi} \ln \left(\frac{k^2}{\mu^2} \right) - i\frac{M}{4}, \quad (15)$$

with $C_0(\mu)$ treated to all orders. For the perturbative calculations presented below, it is useful to expand Eq. (14) formally to third order in the renormalized coupling:

$$\begin{aligned} C_0 &= C_0(\mu) \left\{ 1 - \frac{MC_0(\mu)}{4\pi} \left[\gamma - \ln \pi - \frac{2}{\epsilon} \right] \right. \\ &\quad \left. + \left(\frac{MC_0(\mu)}{4\pi} \left[\gamma - \ln \pi - \frac{2}{\epsilon} \right] \right)^2 + O[C_0(\mu)^3] \right\}. \end{aligned} \quad (16)$$

Now consider matching Eq. (15) to the effective range expansion given in Eq. (5). In order to include effective-range corrections via the C_2 operator, it is convenient to note that in DR all contact interactions can be formally summed to give

$$T_0(k) = -\frac{\sum C_{2n} k^{2n}}{1 - I_0(k) \sum C_{2n} k^{2n}}, \quad (17)$$

with

$$\cot \delta_0(k) = \frac{1}{\text{Im} I_0(k)} \left[\frac{1}{\sum C_{2n} k^{2n}} - \text{Re} I_0(k) \right]. \quad (18)$$

Matching Eq. (15), with the C_2 contribution included, to the effective range expansion then gives the EFT-inspired form:

$$\cot \delta_0(k) = \frac{2}{\pi} \left[\ln \left(\frac{k}{\mu} \right) - \frac{1}{\alpha(\mu)} \right] + \sigma_2 k^2 + O(k^4), \quad (19)$$

where

$$\alpha(\mu) \equiv \frac{MC_0(\mu)}{2\pi} = -\frac{1}{\ln \mu a_2}, \quad \sigma_2 = \frac{4C_2(\mu)}{MC_0(\mu)^2}. \quad (20)$$

As intuited above from general scaling arguments, it is clear that $\alpha(\mu)$ is a dimensionless scale-dependent coupling constant which is the natural expansion parameter in the EFT.

⁸This section closely follows the development in Refs. [38,39].

⁹In DR the couplings are multiplied by $(\frac{\mu}{2})^\epsilon$ to keep the action dimensionless. In the EFT, this is equivalent to multiplying the divergent loop integrals by $(\frac{\mu}{2})^\epsilon$.

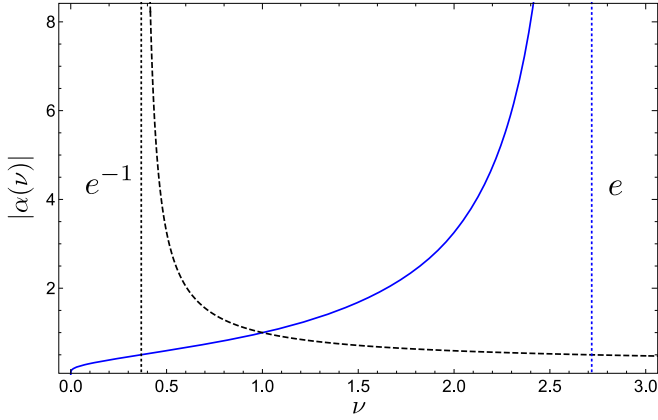


FIG. 3. Running of the coupling with $\mu = 1$ and $|\alpha(1)| = 1$, as described in the text: the solid blue curve corresponds to repulsive coupling, $\alpha(\nu) = |\alpha(\nu)|$, while the dashed black curve corresponds to attractive coupling, $\alpha(\nu) = -|\alpha(\nu)|$. The vertical dotted (blue) line to the right corresponds to the position of the Landau pole at $\nu = e$ in the repulsive case, while the vertical dotted (black) line to the left corresponds to the bound state at $\nu = e^{-1}$ in the attractive case.

Evidently the condition for a bound state, $\cot \delta_0(i\gamma_B) = i$ with binding momentum $\gamma_B > 0$, is satisfied both for attractive coupling, $C_0 < 0$, and for repulsive coupling, $C_0 > 0$. This is due to the strong infrared quantum effects which give rise to the logarithm when C_0 is treated to all orders. Neglecting range corrections, the binding momentum is given by

$$\gamma_B = \mu \exp\left(\frac{1}{\alpha(\mu)}\right) = 1/a_2, \quad (21)$$

with binding energy $\varepsilon_B = -\gamma_B^2/M$.

The RG evolution of $\alpha(\mu)$ clarifies the distinction between attraction and repulsion. Consider the C_0 beta function:

$$\beta(C_0) = \mu \frac{d}{d\mu} C_0(\mu) = \frac{M}{2\pi} C_0(\mu)^2. \quad (22)$$

Solving this equation gives the RG evolution:

$$\alpha(\nu) = \frac{\alpha(\mu)}{1 - \alpha(\mu) \ln\left(\frac{\nu}{\mu}\right)}. \quad (23)$$

In the attractive case, $\alpha(\nu) = -|\alpha(\nu)|$, and the coupling is asymptotically free, whereas in the repulsive case, $\alpha(\nu) = |\alpha(\nu)|$, and the coupling increases monotonically with scale until it hits the Landau pole at $\nu = \mu \exp[1/\alpha(\mu)]$ which coincides with the binding momentum. This is illustrated in Fig. 3 with the choice $\mu = 1$ and $|\alpha(1)| = 1$.¹⁰ One sees that in the repulsive case, the singularity of the S matrix coincides with the position of the Landau pole, which marks the upper limit of the perturbative description in terms of α , and is therefore unphysical. The physical cutoff of the EFT is therefore determined by the smaller of this scale and the scale R^{-1} which characterizes the range of the interaction. In the attractive case, the universal interaction is UV complete, and the EFT is valid below the scale R^{-1} .

¹⁰Note that here natural units are chosen such that $\mu = 1$ corresponds to a typical infrared physical scale of the system.

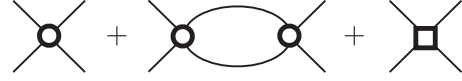


FIG. 4. Leading p -wave contributions to scattering. The empty circle (square) corresponds to an insertion of the C'_2 (C'_4) operator.

C. Scattering in the EFT: p wave

The contribution to the p -wave scattering amplitude up to next-to-leading order (NLO) is given by the sum of Feynman diagrams shown in Fig. 4 which give

$$\begin{aligned} T_1(k, \phi) &= -C'_2 \mathbf{k} \cdot \mathbf{k}' - C_2'^2 M k_i' k_j \left(\frac{\mu}{2}\right)^\epsilon \\ &\times \int \frac{d^{d-1} \mathbf{q}}{(2\pi)^{d-1}} \left(\frac{q_i q_j}{k^2 - q^2 + i\delta} \right) - C'_4 k^2 \mathbf{k} \cdot \mathbf{k}' \\ &= \mathbf{k} \cdot \mathbf{k}' \left[-C'_2 - C_2'^2 \frac{1}{2 - \epsilon} I_1(k) - C'_4 k^2 \right]. \end{aligned} \quad (24)$$

Defining the renormalized coefficient, $C'_4(\mu)$, with \overline{MS} gives

$$C'_4 \equiv C'_4(\mu) - C_2'^2 \frac{M}{8\pi} \left[\gamma - \ln \pi - \frac{2}{\epsilon} - 1 \right], \quad (25)$$

and the renormalized scattering amplitude is then

$$T_1(k, \phi) = \mathbf{k} \cdot \mathbf{k}' \left[-C'_2 - C_2'^2 \frac{M k^2}{8\pi} \ln\left(-\frac{k^2}{\mu^2}\right) - C'_4(\mu) k^2 \right]. \quad (26)$$

Now matching to the scattering amplitude of Eq. (8) gives

$$\sigma_p = \frac{M C_2'}{8}, \quad \alpha_p(\mu) = \frac{4\pi C'_4(\mu)}{M C_2'^2}, \quad (27)$$

where $a_p = \mu^{-1} \exp[\alpha_p(\mu)]$.

A noteworthy feature of the p -wave interaction, which is also the case in three dimensions, is that, if the leading operators, C'_2 and C'_4 , are treated to all orders, then subleading counterterms are required [40]. The highly singular nature of the p -wave interaction renders the all-orders renormalization subtle, and analogous to all-orders renormalization of range corrections in the s wave [41]. In this paper, only the leading order (LO) in the perturbative expansion of the p -wave scattering amplitude will be considered. An important distinction from the s wave is that the leading p -wave effect, due to C'_2 , does not run with the RG in \overline{MS} when one-loop effects are included.

IV. FINITE-DENSITY TECHNOLOGY

A. Ideal gas and in-medium modifications

In two dimensions, the density $\rho = N/A$, with N the number of particles and A the spatial area enclosing the particles, of a noninteracting system with Fermi momentum k_F and degeneracy g is

$$\rho = g \int \frac{d^2 \mathbf{k}}{(2\pi)^2} \theta(k_F - k) = \frac{g k_F^2}{4\pi}. \quad (28)$$

Here, a common Fermi momentum is considered for all spin components, that is, a spin-balanced Fermi gas. With free

single-particle energy $\omega_{\mathbf{k}} \equiv \mathbf{k}^2/(2M)$, the energy density \mathcal{E}_0 of a noninteracting Fermi gas is

$$\mathcal{E}_0 = g \int \frac{d^2\mathbf{k}}{(2\pi)^2} \omega_{\mathbf{k}} \theta(k_F - k) = \rho \frac{1}{2} \frac{k_F^2}{2M}. \quad (29)$$

The energy per particle is $E/N = \mathcal{E}_0/\rho$, and can be written as

$$E/N = \varepsilon_{\text{FG}} = \frac{k_F^2}{4M} = \frac{1}{2} \varepsilon_F, \quad (30)$$

with $\varepsilon_F \equiv k_F^2/(2M)$.

Feynman diagrams can be used to compute the effect of interactions on the energy density, and the relevant Feynman rules can be found in Refs. [7,12]. In particular, the interaction vertices can be read off from Eq. (1) and, for corrections to the energy at weak coupling, internal lines are assigned propagators $iG_0(\tilde{k})_{\alpha\gamma}$, where $\tilde{k} \equiv (k_0, \mathbf{k})$ is the three-momentum assigned to the line, α and γ are spin indices, and

$$\begin{aligned} iG_0(\tilde{k})_{\alpha\gamma} &= iG_0(\tilde{k})\delta_{\alpha\gamma} \\ &= i\delta_{\alpha\gamma} \left(\frac{\theta(k - k_F)}{k_0 - \omega_{\mathbf{k}} + i\delta} + \frac{\theta(k_F - k)}{k_0 - \omega_{\mathbf{k}} - i\delta} \right) \\ &= \delta_{\alpha\gamma} \left(\frac{i}{k_0 - \omega_{\mathbf{k}} + i\delta} - 2\pi\delta(k_0 - \omega_{\mathbf{k}})\theta(k_F - k) \right). \end{aligned} \quad (31)$$

The second line breaks the propagator into ‘‘free’’ and ‘‘in-medium’’ components.

B. In-medium counting scheme

In medium, the free-space power counting of Eq. (2) gets simply modified by setting $E = 0$ which gives

$$\chi = d + 1 + \sum_{n=2}^{\infty} \sum_{i=0}^{\infty} [2i + (d-1)n - d - 1] V_{2i}^n. \quad (32)$$

This contributes to the energy density at order $k_F^\chi R^{\chi-d-1}$ where the powers of R follow from dimensional analysis. For universal interactions (C_0 only), $\chi = d + 1 + (d-3)V_0^2$. Therefore, in three dimensions, $\chi = 5 + V_0^2$ and there is a perturbative expansion with a new power of $k_F R$ accompanying each insertion of C_0 . By contrast, in two dimensions, $\chi = 4$, and the energy density is given by

$$\mathcal{E} = k_F^4 f(\alpha), \quad (33)$$

where f is a function of α such that $\mathcal{E}_0 = k_F^4 f(0)$. In the Fermi-liquid regime considered here, f admits a power series expansion in α , and the goal is to compute

$$\mathcal{E}_{\text{FL}} = \sum_{n=0}^{n_{\text{max}}} \mathcal{E}_n \quad (34)$$

up to n_{max} . This paper will consider $n_{\text{max}} = 3$ corresponding to three orders in α .

C. Thermodynamic potential and superfluid gap

The EFT and power counting outlined above apply to the two-dimensional Fermi gas with weak repulsive coupling α . In the presence of an arbitrarily weak attractive interaction, the BCS mechanism causes the Fermi surface to become unstable. This leads to pairing superfluidity (superconductivity) for neutral (charged) fermions which spontaneously breaks the particle-number symmetry through the formation of a gap, or condensate [42,43]. In making comparisons with numerical simulations in the attractive regime, it is necessary to subtract the contribution to the energy density that arises from the presence of the superfluid gap.¹¹

The superfluid gap in two dimensions was originally computed in Refs. [28,29]. Here the s -wave gap in two dimensions is computed in the \overline{MS} scheme in two ways: by a direct construction and minimization of the renormalized thermodynamic potential, following Ref. [44], and via a direct solution of the self-consistent gap equation [11,45–47].

As long as $C_0 < 0$, it is necessary to treat the interactions which are kinematically enhanced by the BCS mechanism to all orders, in direct violation of the power-counting rules introduced above. For consideration of pairing phenomena, it is convenient to view the EFT somewhat more expansively. Beginning with the effective Lagrangian defined in Eq. (1), with universal interactions only and $g = 2$, one goes to Euclidean space via $t \rightarrow -i\tau$, and $\mathcal{L} \rightarrow -\mathcal{L}_E$ to give

$$\mathcal{L}_E = \psi^\dagger \left[\partial_\tau - \frac{\vec{\nabla}^2}{2M} - \mu_F \right] \psi + \frac{C_0}{2} (\psi^\dagger \psi)^2, \quad (35)$$

and a chemical potential, μ_F , has been introduced for ψ (not to be confused with the DR scale μ). The partition function is then

$$\mathcal{Z} = \int \mathcal{D}\psi \mathcal{D}\psi^\dagger \exp \left[- \int d^3x \mathcal{L}_E \right]. \quad (36)$$

Now if \mathcal{Z} can be computed at finite temperature T , then the thermodynamic potential is known and given by

$$\beta \Omega(A, \mu_F, T) = - \ln \mathcal{Z}(A, \mu_F, T), \quad (37)$$

where A is the area and $\beta \equiv 1/T$ with $k_B = 1$. The solution can be found by introducing a complex auxiliary field $\Phi = C_0 \psi_\uparrow \psi_\downarrow$ which decouples the four-Fermi interaction and whose expectation value gives the superfluid gap. The Euclidean action is now bilinear in the fermion fields and is formally solved in terms of a fermionic determinant.

Neglecting fluctuations in the fields, that is assuming $\Phi = \text{const} \neq 0$, gives the bare thermodynamic potential at zero temperature [44]:

$$\Omega(A, \mu_F, \Phi, \Phi^*) = A \left\{ -\frac{1}{C_0} |\Phi|^2 - \int \frac{d^2q}{(2\pi)^2} \left[\sqrt{(\omega_{\mathbf{q}} - \mu_F)^2 + |\Phi|^2} - (\omega_{\mathbf{q}} - \mu_F) \right] \right\}. \quad (38)$$

¹¹Note that a unified EFT treatment of the weakly attractive Fermi liquid has been developed in Ref. [12].

These divergent integrals may be evaluated with DR using the formula¹²

$$\tilde{I}(\Phi) = \left(\frac{\mu}{2}\right)^\epsilon \int \frac{d^{d-1}\mathbf{q}}{(2\pi)^{d-1}} \frac{1}{\sqrt{(\omega_{\mathbf{q}} - \mu_F)^2 + |\Phi|^2}} = \frac{M}{2\pi} \left[\frac{2}{\epsilon} + \ln\left(\frac{\mu^2\pi}{M\mu_F}\right) - \gamma - \ln\left(\sqrt{1 + |\Phi|^2/\mu_F^2} - 1\right) \right]. \quad (39)$$

Renormalizing with \overline{MS} using Eq. (14), and exchanging the renormalized coupling for the two-body binding energy using Eq. (21) then gives the renormalized thermodynamic potential [44]:

$$\Omega(A, \mu_F, \Phi, \Phi^*) = A \frac{M}{4\pi} |\Phi|^2 \left[\ln \frac{\sqrt{\mu_F^2 + |\Phi|^2} - \mu_F}{|\epsilon_B|} - \frac{\mu_F}{\sqrt{\mu_F^2 + |\Phi|^2} - \mu_F} - \frac{1}{2} \right]. \quad (40)$$

This remarkable formula immediately reveals that the superfluid state is energetically favorable and is intrinsically related to two-body binding [28,29]. The minimum of the potential occurs at $\Phi = \Phi^* = \Delta_{LO}$ and defines the leading-order gap:

$$\Delta_{LO}^2 = \epsilon_B^2 + 2\mu_F |\epsilon_B|. \quad (41)$$

The density is given by

$$\rho = -\frac{1}{A} \frac{\partial \Omega(A, \mu_F, \Phi, \Phi^*)}{\partial \mu_F} = \frac{M}{2\pi} \left(\mu_F + \sqrt{\Delta_{LO}^2 + \mu_F^2} \right) \quad (42)$$

and, after using Eq. (28), results in

$$2\epsilon_F = \mu_F + \sqrt{\mu_F^2 + \Delta_{LO}^2}. \quad (43)$$

Combining Eqs. (21) and (43) gives finally, for $\mu_F > 0$,

$$\Delta_{LO} = \sqrt{2\epsilon_F |\epsilon_B|}, \quad \mu_F = \epsilon_F - \frac{1}{2} |\epsilon_B|, \quad (44)$$

in agreement with Refs. [28,29].

It is instructive to obtain this result using Feynman diagrams as they render in-medium corrections more transparent. The gap equation is shown diagrammatically in Fig. 5 where the C_0 vertex is represented by a dotted line to distinguish which fermion lines are being contracted [48]. This is evaluated to LO by taking the two-particle irreducible potential equal to the tree-level contact vertex, $V_{pp} = C_0$, and using a propagator which accounts for the gap [11,44]. The result is

$$\Delta_{LO} = -C_0 \int \frac{d^3q}{(2\pi)^3} \frac{\Delta_{LO}}{q_3^2 + (\omega_{\mathbf{q}} - \mu_F)^2 + |\Delta_{LO}|^2}, \quad (45)$$

where q_3 is the third component of Euclidean momentum. The gap is the self-consistent solution to this equation, which treats C_0 to all orders even if it is arbitrarily weak because of the kinematical enhancement (BCS instability) of the loop function for $|\mathbf{q}| \sim k_F$. Performing the q_3 integration leaves

$$-\frac{1}{C_0} = \frac{1}{2} \tilde{I}(\Delta_{LO}). \quad (46)$$

Using Eq. (39) and renormalizing with \overline{MS} using Eq. (14) then gives

$$\frac{1}{C_0(\sqrt{M\mu_F})} = \frac{M}{4\pi} \ln \left(\sqrt{1 + \frac{\Delta_{LO}^2}{\mu_F^2}} - 1 \right) \quad (47)$$

which immediately recovers Eq. (41).

The energy density of the paired state is given by

$$\mathcal{E} = A^{-1} \Omega + \mu_F \rho = \mathcal{E}_0 - \frac{M}{4\pi} \Delta_{LO}^2. \quad (48)$$

In the literature this approximation of the energy is denoted mean-field BCS theory. The contribution of the gap to the energy per particle is thus given by [11,47,49–51]

$$(E/N)_\Delta = \frac{1}{2} \epsilon_B. \quad (49)$$

Therefore, evidently the existence of a bound state is a necessary and sufficient condition for the existence of s -wave pairing, in contrast to the three-dimensional case [28,29]. At weak, attractive coupling, the contribution of the gap to the energy is exponentially suppressed, which, as will be seen, allows a meaningful perturbative expansion in α .

The NLO contribution to the gap takes into account the particle-hole (“ring”) correction to the two-particle irreducible potential V_{pp} [11,47,49–51] as shown in the bottom of Fig. 5. This accounts for the polarizability of the finite-density medium which effectively screens the contact interaction. For the kinematics which lead to the BCS instability, $\mathbf{k}_1 = -\mathbf{k}_2 \equiv \mathbf{k}$, $\mathbf{k}'_1 = -\mathbf{k}'_2 \equiv \mathbf{k}'$, and $k = k' = k_F$, the potential may be

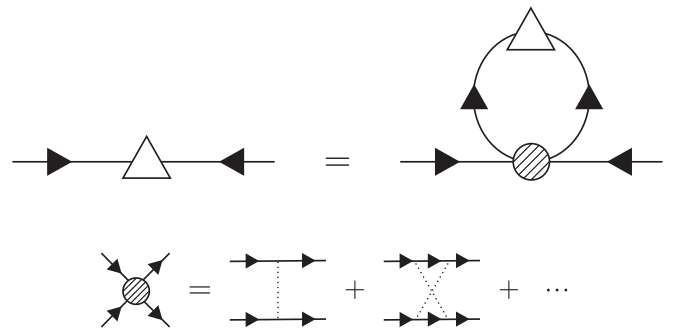


FIG. 5. Top: The gap equation diagrammatically, with the empty triangle denoting an insertion of the gap. Bottom: The shaded circle represents an insertion of the two-particle irreducible potential $-iV_{pp}$, with the dotted lines denoting a C_0 interaction. Crossed diagrams and diagrams which cancel are not shown.

¹²Note that one may take a derivative of the integral with respect to $|\Phi|$, evaluate using DR, and then integrate with respect to $|\Phi|$.

computed in the gapless EFT with $k_F R \ll 1$ to give

$$V_{pp} = C_0(\delta_{\alpha\gamma}\delta_{\beta\delta} - \delta_{\alpha\delta}\delta_{\beta\gamma}) + iC_0^2 \int \frac{d^3q}{(2\pi)^3} [G_0(\tilde{q}) G_0(\tilde{q} + \tilde{P}_+) \delta_{\alpha\gamma}\delta_{\beta\delta} - G_0(\tilde{q}) G_0(\tilde{q} + \tilde{P}_-) \delta_{\alpha\delta}\delta_{\beta\gamma}] \quad (50)$$

where $\tilde{P}_\pm = (0, \mathbf{k} \pm \mathbf{k}')$. Spin indices have temporarily been restored and α, β (γ, δ) are the spin indices of the incoming (outgoing) particles. To project the potential onto the s wave one must integrate over all $\cos \theta = \hat{\mathbf{k}} \cdot \hat{\mathbf{k}}'$. However, it is straightforward to show that V_{pp} computed to one loop contains no partial waves higher than $\ell = 0$ [52]. Therefore the two terms with \tilde{P}_\pm contribute equally to V_{pp} which becomes

$$V_{pp} = C_0 + 2MC_0^2 \int_{q < k_F} \frac{d^2\mathbf{q}}{(2\pi)^2} \left[\frac{1}{P_-^2/2 + \mathbf{q} \cdot \mathbf{P}_- - i\epsilon} + i\pi \delta(P_-^2/2 + \mathbf{q} \cdot \mathbf{P}_-) \theta(k_F - |\mathbf{q} + \mathbf{P}_-|) \right], \quad (51)$$

where spin indices have again been suppressed. Evaluating the integral¹³ results in

$$V_{pp} = C_0 + \frac{M}{2\pi} C_0^2. \quad (52)$$

The gap equation then becomes

$$-\frac{1}{C_0} \left(1 + \frac{M}{2\pi} C_0 \right)^{-1} = -\frac{1}{C_0} + \frac{M}{2\pi} + O(C_0) = \frac{1}{2} \tilde{I}(\Delta_{\text{NLO}}). \quad (53)$$

Neglecting the $O(C_0)$ corrections on the left-hand side then leads to the gap energy up to NLO,

$$\Delta_{\text{NLO}} = \frac{1}{e} \Delta_{\text{LO}}, \quad (54)$$

in agreement with Ref. [50].

As the omitted corrections to V_{pp} are $O(C_0^3)$, one expects that Eq. (54) is valid up to corrections of $O(\alpha \Delta_{\text{NLO}})$. It is important to stress that while the computation of the gap is valid for all interparticle separations k_F^{-1} , the EFT giving rise to this screening correction is strictly valid at large interparticle separations. Indeed, at strong coupling, the paired fermions are expected to become tightly bound, leading to the BCS-BEC crossover to a gas of repulsive bosons. Clearly, in this limit, screening effects will become negligible as the diameter of the pair will be much smaller than k_F^{-1} , and therefore it is expected that the LO gap contribution to the energy per particle, $\varepsilon_B/2$, will be exact. Notice, however, that mean-field BCS theory in the strong-coupling molecular limit misses the correct interaction energy between composite bosons [20,50]. In particular, the first term in Eq. (48) is not correct in the BEC limit, because it should include the interaction energy of the composite bosons.



FIG. 6. Leading-order diagram (the bow tie) contributing to the energy density. The black circle corresponds to an insertion of the C_0 operator.

V. WEAKLY COUPLED FERMİ GAS: UNIVERSAL CORRECTIONS

A. Fermi-liquid regimes

The goal in what follows is to compute the energy density in the weak-coupling, Fermi-liquid regime, $|\alpha| \ll 1$, which has been shown to divide into a repulsive and an attractive branch as

$$\mathcal{E} = \begin{cases} \mathcal{E}_{\text{FL}}, & \alpha > 0 \\ \mathcal{E}_{\text{FL}} - \frac{M}{4\pi} \Delta^2, & \alpha < 0, \end{cases} \quad (55)$$

where $\Delta = \Delta_{\text{NLO}}[1 + O(\alpha)]$. Note that although the energy due to pairing is exponentially small in $|\alpha|$, it is included in order to be able to consistently compare with the Monte Carlo simulations. In what follows the perturbative calculation of \mathcal{E}_{FL} in powers of α is described order by order.

B. Leading order

The LO diagram which contributes to the energy density, \mathcal{E}_{FL} , is shown in Fig. 6 and yields

$$\mathcal{E}_1 = \frac{1}{2} C_0 g(g-1) \left(\lim_{\eta \rightarrow 0^+} \int \frac{d^3k}{(2\pi)^3} e^{ik_0\eta} iG_0(\tilde{k}) \right)^2. \quad (56)$$

The dk_0 integration is performed using contour integration, which picks up the $\theta(k_F - k)$ pole, and the remaining d^2k integral up to k_F is trivial. The result is

$$\mathcal{E}_1 = \rho(g-1) \frac{k_F^2}{8\pi} C_0, \quad (57)$$

and is sometimes referred to as the mean-field contribution. Using Eq. (16) to replace the bare coupling with the renormalized coupling, and using Eq. (20) to express the final result in terms of α , it is found that

$$\mathcal{E}_1 = \rho(g-1) \frac{k_F^2}{4M} \{ \alpha(\mu) + O[\alpha(\mu)^2] \}. \quad (58)$$

At this order, the RG scale is arbitrary and will be set once the NLO contributions are taken into account. The factor of $g-1$ will be common to all universal corrections and reflects that this interaction must vanish for single-component fermions due to Pauli statistics.

C. Next-to-leading order

The NLO calculations in this section and the NNLO calculations in the following section reproduce the results first found in Refs. [16,17]. The nominal NLO corrections come from the diagrams in Fig. 7. Figure 7(b) is ‘‘anomalous’’ and

¹³This integral appears in the NNLO correction to the energy density and is evaluated below [see Eq. (79)].

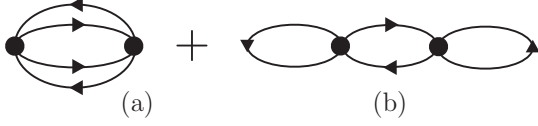


FIG. 7. Next-to-leading-order diagrams contributing to the energy density. Only diagram (a), the beach ball diagram, is nonvanishing.

is identically zero. The contribution from Fig. 7(a), the beach ball diagram, is

$$\begin{aligned} \mathcal{E}_2 = & -i \frac{C_0^2}{4} g(g-1) \int \frac{d^3 p_1}{(2\pi)^3} \int \frac{d^3 p_2}{(2\pi)^3} \\ & \times \int \frac{d^3 k}{(2\pi)^3} G_0(\tilde{p}_1) G_0(\tilde{p}_2) G_0(\tilde{P} + \tilde{k}) G_0(\tilde{P} - \tilde{k}), \end{aligned} \quad (59)$$

where $\tilde{P} = (\tilde{p}_1 + \tilde{p}_2)/2$ and it is convenient to define $\tilde{q} = (\tilde{p}_1 - \tilde{p}_2)/2$. Using the in-medium form of the propagator, it is found that only terms with two in-medium insertions on either side of a loop survive the contour integration. Without loss of generality, the two in-medium insertions may be placed on the $\tilde{p}_{1,2}$ loop. This puts $\tilde{p}_{1,2}$ on shell and restricts their momenta to be below the Fermi surface. After performing the contour integrals, the energy becomes

$$\mathcal{E}_2 = \frac{MC_0^2}{4} g(g-1) \int_{p_{1,2} < k_F} \frac{d^2 \mathbf{p}_1 d^2 \mathbf{p}_2}{(2\pi)^4} [2\mathcal{I}_0 + 2\mathcal{I}_1 + \mathcal{I}_2], \quad (60)$$

where

$$\mathcal{I}_0 = \left(\frac{\mu}{2}\right)^\epsilon \int \frac{d^{d-1} \mathbf{k}}{(2\pi)^{d-1}} \frac{1}{q^2 - k^2 + i\delta}, \quad (61)$$

$$\mathcal{I}_1 = - \int \frac{d^2 \mathbf{k}}{(2\pi)^2} \frac{\theta(k_F - |\mathbf{P} + \mathbf{k}|) + \theta(k_F - |\mathbf{P} - \mathbf{k}|)}{q^2 - k^2 + i\delta}, \quad (62)$$

$$\begin{aligned} \mathcal{I}_2 = & -2i\pi \int \frac{d^2 \mathbf{k}}{(2\pi)^2} \delta(k^2 - q^2) \theta(k_F - |\mathbf{P} - \mathbf{k}|) \\ & \times \theta(k_F - |\mathbf{P} + \mathbf{k}|), \end{aligned} \quad (63)$$

and \overline{MS} is used to define $\mathcal{I}_0 [= I_0(q)/M]$. The energy is manifestly real and, for $p_{1,2} < k_F$,

$$\text{Im}(2\mathcal{I}_0 + 2\mathcal{I}_1 + \mathcal{I}_2) = 0. \quad (64)$$

After changing to dimensionless variables, $s = P/k_F$ and $t = q/k_F$, the real parts are found to be

$$\begin{aligned} \text{Re } \mathcal{I}_0 = & \frac{1}{4\pi} \left[\ln \left(\frac{t^2 k_F^2}{\mu^2} \right) + \gamma - \ln \pi - \frac{2}{\epsilon} \right], \\ \text{Re } \mathcal{I}_1 = & -\frac{1}{2\pi} [\ln t - H(s, t)], \end{aligned} \quad (65)$$

where [16]

$$\begin{aligned} H(s, t) = & 2\theta(1-s-t) \ln \frac{\sqrt{1-(s+t)^2} + \sqrt{1-(s-t)^2}}{2\sqrt{t}} \\ & + \theta(s+t-1) \ln s. \end{aligned} \quad (66)$$

After integrating by parts, the following identity is obtained:

$$\begin{aligned} & \int_{p_{1,2} < k_F} \frac{d^2 \mathbf{p}_1 d^2 \mathbf{p}_2}{(2\pi)^4} f(s, t) \\ & = \frac{2k_F^4}{\pi^3} \int_0^1 ds s \int_0^{\sqrt{1-s^2}} dt t J(s, t) f(s, t) \end{aligned} \quad (67)$$

where $f(s, t)$ is an arbitrary function and

$$J(s, t) = \frac{\pi}{2} \theta(1-s-t) + \theta(s+t-1) \arcsin \frac{1-s^2-t^2}{2st}. \quad (68)$$

Applying this to Eq. (60), one finds

$$\begin{aligned} \mathcal{E}_2 = & MC_0^2 g(g-1) \frac{k_F^4}{\pi^3} \int_0^1 ds s \\ & \times \int_0^{\sqrt{1-s^2}} dt t J(s, t) [\text{Re } \mathcal{I}_0 + \text{Re } \mathcal{I}_1]. \end{aligned} \quad (69)$$

Notice that the $\ln(t)$ term cancels in the integrand and the remaining integration over $\text{Re } \mathcal{I}_0$ in Eq. (69) gives

$$\delta \mathcal{E}_2 = \rho(g-1) \frac{k_F^2}{8\pi} \frac{C_0^2 M}{4\pi} \left[\ln \left(\frac{k_F^2}{\mu^2} \right) + \gamma - \ln \pi - \frac{2}{\epsilon} \right]. \quad (70)$$

Adding this contribution to the LO energy density, choosing $\mu = k_F$, and replacing the bare parameters with renormalized parameters using Eq. (16), one finds

$$\mathcal{E}_1 + \delta \mathcal{E}_2 = \rho(g-1) \frac{k_F^2}{8\pi} C_0(k_F) + O[C_0(k_F)^3]. \quad (71)$$

The integration over \mathcal{I}_1 in Eq. (69) gives

$$\delta \mathcal{E}'_2 = \rho(g-1) \frac{k_F^2}{16\pi^2} MC_0^2 \left(\frac{3}{4} - \ln 2 \right). \quad (72)$$

Again, using Eq. (16) to renormalize this contribution, and with $\mathcal{E}_2 = \delta \mathcal{E}_2 + \delta \mathcal{E}'_2$, one finds to NLO

$$\begin{aligned} \mathcal{E}_1 + \mathcal{E}_2 = & \rho(g-1) \frac{k_F^2}{4M} \left[\alpha(k_F) + \alpha(k_F)^2 \left(\frac{3}{4} - \ln 2 \right) \right. \\ & \left. + O[\alpha(k_F)^3] \right], \end{aligned} \quad (73)$$

where Eq. (20) has been used to express the final result in terms of α . This recovers the result of Refs. [25,26]. Note that $3/4 - \ln 2 = 0.05685$ is small as compared to a number of order 1. The small size of this correction has been observed in comparison with MC simulations [19], which suggest a stronger deviation from the mean-field result, and motivates the study of higher-order effects.

D. Next-to-next-to-leading order

The NNLO corrections come from the diagrams in Fig. 8. Figures 8(c)–(e) are all anomalous and evaluate to zero. The ladder diagram, Fig. 8(a), gives a logarithmically-divergent contribution to the energy:

$$\begin{aligned} \mathcal{E}_3^L = & g(g-1) \frac{C_0^3}{6} \int \frac{d^3 p_1}{(2\pi)^3} \int \frac{d^3 p_2}{(2\pi)^3} G_0(\tilde{p}_1) G_0(\tilde{p}_2) \\ & \times \left[\int \frac{d^3 k}{(2\pi)^3} G_0(\tilde{P} + \tilde{k}) G_0(\tilde{P} - \tilde{k}) \right]^2. \end{aligned} \quad (74)$$

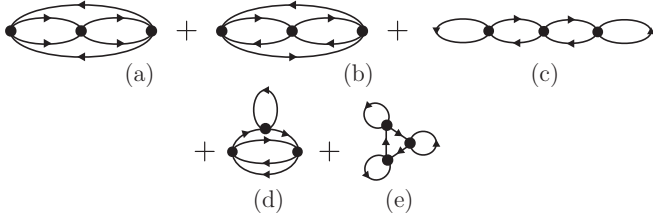


FIG. 8. Next-to-next-to-leading-order diagrams contributing to the energy density. Only diagrams (a) and (b) are nonvanishing.

As with the beach ball diagram, only terms with two in-medium insertions on either side of a loop are nonzero and

these will again be placed on the $\tilde{p}_{1,2}$ loop. Many of the nonvanishing terms are identical due to the cyclic symmetry of the diagram and the integrals involved are the same as in the evaluation of the beach ball. Here, the imaginary parts will need to be kept and the following relation is particularly useful:

$$\text{Im}(\mathcal{I}_0 + \mathcal{I}_1 + \mathcal{I}_2) = \frac{\mathcal{I}_2}{2i} = -\frac{J(s, t)}{2\pi}, \quad (75)$$

which holds for $s^2 + t^2 < 1$. After performing the contour integration, the energy reads

$$\begin{aligned} \mathcal{E}_3^L &= g(g-1) \frac{C_0^3}{6} M^2 \int_{p_{1,2} < k_F} \frac{d^2 \mathbf{p}_1 d^2 \mathbf{p}_2}{(2\pi)^4} [3(\mathcal{I}_0 + \mathcal{I}_1 + \mathcal{I}_2)^2 - \mathcal{I}_2(3\mathcal{I}_0 + 3\mathcal{I}_1 + 2\mathcal{I}_2)] \\ &= \frac{\rho(g-1)C_0^3 M^2 k_F^2}{3\pi^4} \int_0^1 ds s \int_0^{\sqrt{1-s^2}} dt t J(s, t) \left\{ -J(s, t)^2 + 3H(s, t)^2 + 3H(s, t) \left[\gamma - \ln \pi - \frac{2}{\epsilon} + \ln(k_F^2/\mu^2) \right] \right. \\ &\quad \left. + \frac{3}{4} \left[\gamma - \ln \pi - \frac{2}{\epsilon} + \ln(k_F^2/\mu^2) \right]^2 \right\}, \end{aligned} \quad (76)$$

where in the second line, Eqs. (65), (67), and (75) have been used. Replacing the bare coupling with the renormalized coupling in $\mathcal{E}_1 + \mathcal{E}_2 + \mathcal{E}_3^L$, and setting $\mu = k_F$ to remove the RG scale dependence at this order, results in

$$\mathcal{E}_3^L = \rho(g-1) \frac{k_F^2}{4M} \left[\alpha(k_F)^3 (0.16079) + O[\alpha(k_F)^4] \right], \quad (77)$$

where the integrals over J^3 and JH^2 have been performed numerically. This is in agreement with the result of Appendix A of Ref. [16].

The ring diagram, Fig. 8(b), gives the finite result

$$\mathcal{E}_3^R = -\frac{i}{6} g(g-1)(g-3) C_0^3 \int \frac{d^3 P}{(2\pi)^3} \left[i \int \frac{d^3 k}{(2\pi)^3} G_0(\vec{k}) G_0(\vec{k} + \vec{P}) \right]^3. \quad (78)$$

After performing the contour integration, the term in brackets becomes

$$\mathcal{I}_R = M \int \frac{d^2 \mathbf{k}}{(2\pi)^2} \left[\left(\frac{\theta(k_F - k)}{P^2/2 + \mathbf{k} \cdot \mathbf{P} - MP_0 - i\delta} + P_0 \rightarrow -P_0 \right) - 2i\pi \delta(MP_0 - P^2/2 - \mathbf{k} \cdot \mathbf{P}) \theta(k_F - k) \theta(k_F - |\mathbf{k} + \mathbf{P}|) \right]. \quad (79)$$

It is convenient to calculate the real and imaginary parts separately. The imaginary part has three terms which, after the change of variables $\mathbf{k} \rightarrow \mathbf{k} - \mathbf{P}/2$, give

$$\begin{aligned} \text{Im } \mathcal{I}_R &= M\pi \int \frac{d^2 \mathbf{k}}{(2\pi)^2} \delta(MP_0 - \mathbf{k} \cdot \mathbf{P}) [\theta(k_F - |\mathbf{k} - \mathbf{P}/2|) \\ &\quad + \theta(k_F - |\mathbf{k} + \mathbf{P}/2|) - 2\theta(k_F - |\mathbf{k} - \mathbf{P}/2|) \\ &\quad \times \theta(k_F - |\mathbf{k} + \mathbf{P}/2|)] \\ &= \frac{M}{4\pi} I(\bar{\nu}, x) \end{aligned} \quad (80)$$

where [17]

$$\begin{aligned} I(\bar{\nu}, x) &= \frac{1}{x} \sqrt{1 - (x - \bar{\nu})^2}, \quad \text{for } |x - 1| < \bar{\nu} < x + 1, \\ I(\bar{\nu}, x) &= \frac{1}{x} [\sqrt{1 - (x - \bar{\nu})^2} - \sqrt{1 - (x + \bar{\nu})^2}], \\ &\quad \text{for } 0 < \bar{\nu} < 1 - x, \end{aligned} \quad (81)$$

and dimensionless variables, $x = P/(2k_F)$ and $2x\bar{\nu} = MP_0/k_F^2$, have been defined. Before calculating the real part, notice that \mathcal{E}_3^R must be proportional to $\text{Im}(\mathcal{I}_R)^3$ to be real, and therefore will always include at least one factor of $I(\bar{\nu}, x)$. Therefore, $\text{Re } \mathcal{I}_R$ need only be defined in the semi-infinite strip where $I(\bar{\nu}, x)$ has support (Fig. 2 in Ref. [17]). In this domain

$$\text{Re } \mathcal{I}_R = \frac{M}{4\pi} R(\bar{\nu}, x) \quad (82)$$

where

$$\begin{aligned} R(\bar{\nu}, x) &= 2 - \frac{1}{x} \sqrt{(x + \bar{\nu})^2 - 1}, \\ &\quad \text{for } |x - 1| < \bar{\nu} < x + 1, \\ R(\bar{\nu}, x) &= 2, \quad \text{for } 0 < \bar{\nu} < 1 - x, \quad 0 < x < 1. \end{aligned} \quad (83)$$

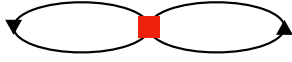


FIG. 9. Effective range contribution to the energy density. The red square corresponds to an insertion of the C_2 operator.

The energy density is then

$$\begin{aligned} \mathcal{E}_3^R &= -\frac{i}{6}g(g-1)(g-3)C_0^3 \int \frac{d^3P}{(2\pi)^3} (\mathcal{I}_R)^3 \\ &= \rho(g-1)(g-3)k_F^2 \frac{C_0^3 M^2}{24\pi^4} \int_0^\infty dx x^2 \\ &\quad \times \int_{\bar{v}_{\min}}^{x+1} d\bar{v} [3R(\bar{v}, x)^2 I(\bar{v}, x) - I(\bar{v}, x)^3], \end{aligned} \quad (84)$$

where $\bar{v}_{\min} = \max(0, x-1)$. Evaluating the integral¹⁴ and setting the RG scale to k_F then gives

$$\mathcal{E}_3^R = \rho(g-1)(g-3) \frac{k_F^2}{4M} \left\{ \alpha(k_F)^3 (2 \ln 2 - 1) + O[\alpha(k_F)^4] \right\}. \quad (85)$$

Finally, the complete NNLO expression is given by

$$\begin{aligned} \mathcal{E}_1 + \mathcal{E}_2 + \mathcal{E}_3^L + \mathcal{E}_3^R \\ &= \rho(g-1) \frac{k_F^2}{4M} \left[\alpha(k_F) + \alpha(k_F)^2 \left(\frac{3}{4} - \ln 2 \right) \right. \\ &\quad \left. + \alpha(k_F)^3 [0.16079 + (g-3)(2 \ln 2 - 1)] \right. \\ &\quad \left. + O[\alpha(k_F)^4] \right]. \end{aligned} \quad (86)$$

Note that with $g=2$, $0.16079 - (2 \ln 2 - 1) = -0.22550$, which is a factor of 4 larger in magnitude than the $\alpha(k_F)^2$ coefficient.

VI. WEAKLY COUPLED FERMI GAS: NONUNIVERSAL CORRECTIONS

A. Range corrections

According to the power-counting formula, Eq. (32), an insertion of the C_2 operator gives an $O(k_F^6)$ contribution to the energy density. However, effective range corrections, and indeed corrections from all orders in the effective range expansion, are also driven by the C_0 operator and therefore will be doubly suppressed in the dilute and weak-coupling limits. From the diagram in Fig. 9,

$$\mathcal{E}_2^{\sigma_2} = \rho(g-1) \frac{k_F^4}{32\pi} C_2, \quad (87)$$

¹⁴The final integration is simpler if one uses rotated coordinates, $x = (\xi + \eta)/2$, $\bar{v} = (\xi - \eta)/2$ where the integration region is $-\xi < \eta < \xi$, $0 < \xi < 1$ and $-1 < \eta < 1$, $\xi > 1$.

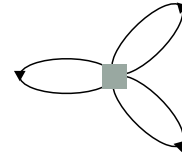


FIG. 10. Leading three-body contribution to the energy density. The gray square corresponds to an insertion of the D_0 operator.

and finally, in terms of renormalized parameters and the two-dimensional effective range defined in Eq. (20),

$$\mathcal{E}_2^{\sigma_2} = \rho(g-1) \frac{k_F^2}{4M} \alpha(k_F)^2 \frac{\pi}{8} (\sigma_2 k_F^2). \quad (88)$$

B. Three-body effects

From the diagram in Fig. 10,

$$\mathcal{E}_0^{D_0} = \rho(g-2)(g-1) \frac{k_F^4}{96\pi^2} D_0, \quad (89)$$

and finally

$$\mathcal{E}_0^{D_0} = \rho(g-2)(g-1) \frac{k_F^2}{4M} \frac{1}{24\pi^2} (MD_0 k_F^2). \quad (90)$$

This scales with the Fermi momentum like a range correction, but with no additional suppression in α . As a local three-body interaction, it vanishes for $g < 3$ due to Pauli statistics.

C. P -wave corrections

From the diagram in Fig. 11,

$$\mathcal{E}_0^{\sigma_p} = \rho(g+1) \frac{k_F^4}{32\pi} C_2', \quad (91)$$

and finally, using Eq. (27),

$$\mathcal{E}_0^{\sigma_p} = \rho(g+1) \frac{k_F^2}{4M} \frac{1}{\pi} (\sigma_p k_F^2). \quad (92)$$

This again scales with the Fermi momentum like a range correction, but with no additional suppression in α , and no longer vanishes for $g=1$ due to the p -wave wave function being antisymmetric.

VII. GENERAL SCALE-DEPENDENT FORM AND THE CONTACT

The energy per particle of the weakly coupled Fermi gas in two dimensions including contributions of $O(\alpha^3)$ and $O(k_F^2)$ in the universal interaction and nonuniversal interactions of



FIG. 11. P -wave contribution to the energy density. The empty circle corresponds to an insertion of the C_2' operator.

$O(k_F^4)$ is

$$E_{\text{FL}}/N = \mathcal{E}_{\text{FL}}/\rho = \varepsilon_{\text{FG}} \left[1 + (g-1)\alpha + (g-1)\alpha^2 \left(\frac{3}{4} - \ln 2 + \frac{\pi}{8} \sigma_2 k_F^2 \right) + (g-1)\alpha^3 [0.16079 + (g-3)(\ln 4 - 1)] \right. \\ \left. + (g+1) \frac{1}{\pi} (\sigma_p k_F^2) + (g-2)(g-1) \frac{1}{24\pi^2} (MD_0 k_F^2) \right], \quad (93)$$

where $\alpha \equiv \alpha(k_F)$. Omitting nonuniversal effects, it is convenient to use the RG evolution of α , via Eq. (23), to express the energy in terms of the arbitrary scale λk_F , where λ is an arbitrary real number.¹⁵ One obtains

$$E_{\text{FL}}/N = \varepsilon_{\text{FG}} \left\{ 1 + (g-1)\alpha(\lambda k_F) + (g-1)\alpha(\lambda k_F)^2 \left(\frac{3}{4} - \ln 2\lambda \right) + (g-1)\alpha(\lambda k_F)^3 [0.16079 + (g-3)(\ln 4 - 1)] \right. \\ \left. - \left(\frac{3}{2} - \ln 4\lambda \right) \ln \lambda \right\} + O[\alpha(\lambda k_F)^4], \quad (94)$$

with

$$\alpha(\lambda k_F) = -[\ln(\lambda k_F a_2)]^{-1}. \quad (95)$$

Note that

$$\lambda \frac{d}{d\lambda} E_{\text{FL}}/N = O[\alpha(\lambda k_F)^4], \quad (96)$$

and therefore any choice of λ leads to the same physical prediction at the order in α computed. However, it is convenient to choose λ to be consistent with the relevant physical scales and optimize perturbation theory. Below, the variation in λ will be used to estimate the uncertainty due to neglecting higher orders in the perturbative expansion.

The contact [53–55] is an observable of short-range interacting gases relating the derivative of the energy with respect to the coupling constant to various static and thermodynamic properties, such as the large momentum tail of the momentum distribution or the high-frequency tail of relevant spectral functions. The theoretical and experimental determination of the contact has thus become a stringent test of internal consistency. Here the s -wave¹⁶ contact density is defined as

$$C = 2\pi M \frac{d\mathcal{E}}{d \ln k_F a_2} = 2\pi M \frac{d(\rho E/N)}{d \ln k_F a_2}. \quad (97)$$

In order to compare the prediction from Fermi-liquid theory with MC simulation it is convenient to define the contact with gap subtracted as C_{FL} . Keeping universal interactions and assuming $g = 2$ (two-component fermions) gives

$$C_{\text{FL}}/k_F^4 = \frac{1}{4} \alpha^2 \left[1 + \left(\frac{3}{2} - \ln 4 \right) \alpha \right. \\ \left. + 3[0.16079 - (\ln 4 - 1)] \alpha^2 + O(\alpha^3) \right]. \quad (98)$$

This is plotted in Fig. 12 where the gray shaded band corresponds to varying the RG scale by 10% around the Fermi surface, i.e., $\lambda = 1 \pm 0.05$. The comparison with MC simulations is discussed in Sec. IX.

¹⁵Note that the expression for the energy density with arbitrary λ is precisely the expression that would have been obtained if the scale μ had been kept arbitrary throughout the perturbative calculation.

¹⁶Contacts for the p -wave interaction and for the effective range may also be defined [56–61].

VIII. LADDERS AND RINGS TO ALL ORDERS

There have been many efforts to treat classes of diagrams to all orders in the interaction strength α , particularly in the case of three dimensions [62], where such resummations provide some insight regarding the energy density of the Fermi gas at unitarity [6,10,11,13,14,16].

The complete ladder and ring diagram resummations have been computed for the Fermi gas in two dimensions in Appendix A of Ref. [16] and in Ref. [17], respectively, and the results will be reproduced here for the purpose of comparison with MC simulations. Figure 13 provides a schematic illustration of the ladder and ring diagrams. The resummed energy density is

$$E_{\text{FL}}/N = \varepsilon_{\text{FG}} [1 + \mathbf{L}(\alpha) + \alpha^3 \mathbf{R}(\alpha)] \\ = \varepsilon_{\text{FG}} \left\{ 1 + \alpha + \alpha^2 \left(\frac{3}{4} - \ln 2 \right) \right. \\ \left. + \alpha^3 [\mathbf{R}(\alpha) + \tilde{\mathbf{L}}(\alpha)] \right\}, \quad (99)$$

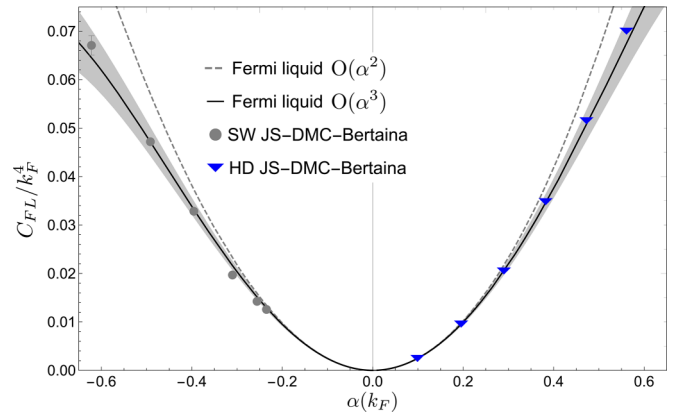


FIG. 12. The contact density, C_{FL} in units of k_F^4 , vs coupling strength. The gray dashed curve is derived from the $O(\alpha^2)$ Fermi-liquid energy and the solid black curve is from $O(\alpha^3)$. The gray band corresponds to varying the RG scale in the $O(\alpha^3)$ Fermi-liquid energy and is a measure of the uncertainty associated with truncating the perturbative expansion, as discussed in the text. Note that the MC data have the gap contribution removed.

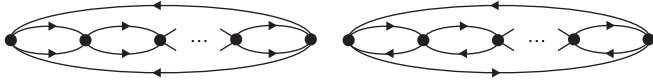


FIG. 13. Schematic representation of ladder diagrams to all orders (left) and ring diagrams to all orders (right). The black circle corresponds to an insertion of the C_0 operator.

where [16]

$$\mathbf{L}(\alpha) = -\frac{32}{\pi} \int_0^1 ds s \int_0^{\sqrt{1-s^2}} dt t \arctan \frac{J(s, t)}{H(s, t) - \alpha^{-1}}, \quad (100)$$

$\tilde{\mathbf{L}}(\alpha)$ is defined by Eq. (99), and

$$\mathbf{R}(\alpha) = -\frac{16}{\alpha^3 \pi} \int_0^\infty dx x^2 \int_{\bar{v}_{\min}}^{x+1} d\bar{v} \left\{ \alpha I(\bar{v}, x) [\alpha R(\bar{v}, x) + 1] + \arctan \frac{\alpha I(\bar{v}, x)}{\alpha R(\bar{v}, x) + 2} + 3 \arctan \frac{\alpha I(\bar{v}, x)}{\alpha R(\bar{v}, x) - 2} \right\}, \quad (101)$$

where $\bar{v}_{\min} = \max(0, x - 1)$, and $I(\bar{v}, x)$ and $R(\bar{v}, x)$ are defined above [17]. This ring function satisfies the asymptotic conditions $\mathbf{R}(\pm\infty) = -1/6$, and both the ladder and ring functions and their sum are plotted in Fig. 14. Note that the resummed energy density agrees with the perturbative expansion up to $O(\alpha^3)$. It is therefore somewhat indicative of the uncertainty associated with the truncation of the perturbative expansion, as will be seen below. Beyond that, its implications, while interesting, are evidently academic and aspirational.

IX. COMPARISON WITH MONTE CARLO SIMULATIONS

Numerical simulations of the energy density of the two-dimensional Fermi gas in the weakly repulsive regime, and from the weakly attractive BCS regime to the strongly coupled BEC regime, using MC techniques, have been carried out in Refs. [19–24,63,64]. The original study by Bertaina and Giorgini [19] used fixed-node diffusion Monte Carlo

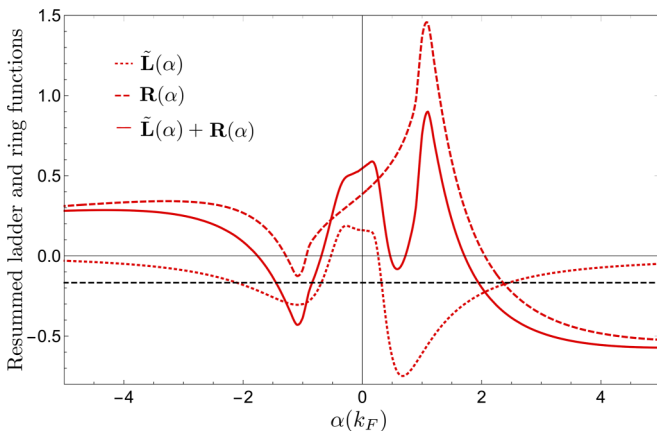


FIG. 14. Resummed ladder and ring functions, $\tilde{\mathbf{L}}(\alpha)$ and $\mathbf{R}(\alpha)$, respectively, and their sum, vs coupling strength. The dashed black line is the asymptotic value of the ring function, $-1/6$.

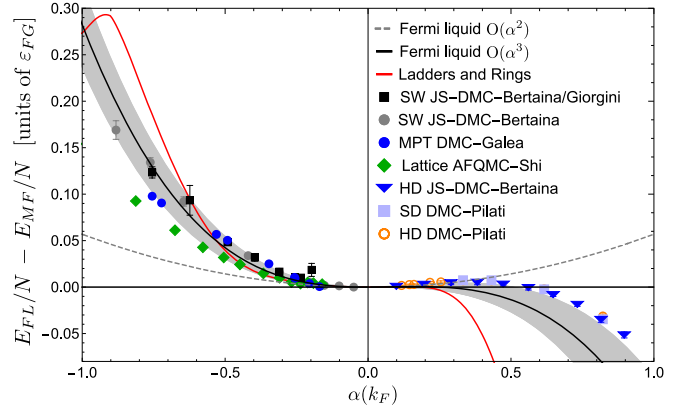


FIG. 15. Energy per particle with mean-field piece subtracted vs coupling strength. The gray dashed curve is NLO and the solid black curve is NNLO. The gray band corresponds to varying the RG scale at NNLO and is a measure of the uncertainty associated with truncating the perturbative expansion, as discussed in the text. The red curve is the complete ladder and ring resummation. The MC data are as described in the text.

(DMC). This study was then augmented by Bertaina [20], who increased the statistics in the attractive branch, and also considered the repulsive branch. Dramatic improvements were then carried out by Shi *et al.* [21], who used auxiliary-field diffusion Monte Carlo (AFDMC), and achieved a more accurate nodal surface (guiding wave function). The results of Shi *et al.* were then largely confirmed by Galea *et al.* [22], who used fixed-node DMC with a refined nodal surface.

With $g = 2$ and omitting for now range corrections and other nonuniversal effects, which are mostly negligible in the simulations, one has from Eq. (93) the prediction

$$E_{\text{FL}}/N = \varepsilon_{\text{FG}} [1 + \alpha + \alpha^2(0.05685) - \alpha^3(0.22550) + O(\alpha^4)]. \quad (102)$$

It is useful to define the mean-field contribution as $E_{\text{MF}}/N = \varepsilon_{\text{FG}}[1 + \alpha]$. Figure 15 plots the energy per particle with the mean-field contribution subtracted and shows that including the $O(\alpha^3)$ contribution does indeed restore the agreement between theory and MC simulation on the attractive side. Figure 16 magnifies this comparison for small negative α . Note that all simulation data shown in the figures in the attractive regime have the NLO gap energy subtracted, as is necessary to compare with the Fermi-liquid predictions, as discussed above and indicated in Eq. (55). In most MC simulation papers, the energy density is expressed as a function of $\ln(k_F a_{2D}) = \ln(k_F a_2) - \gamma + \ln 2$, and therefore one must either translate between the two scattering length conventions or use the freedom in changing the RG scale to achieve the same effect. The gray shaded band again corresponds to varying the RG scale by $\lambda = 1 \pm 0.05$. The red curve is the complete ladder and ring diagram sum.

Galea *et al.* [22] obtain smaller energies than Bertaina and Giorgini [19] as the coupling increases, a reflection of the more accurate nodal surface. Because fixed-node DMC is a variational method, it is expected that the lower energies provide a more accurate calculation of the ground state. The method used by Shi *et al.* [21], AFDMC, is free of the sign

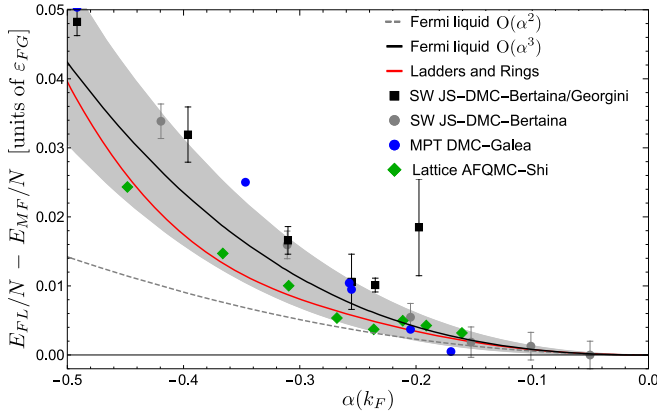


FIG. 16. Energy per particle with mean-field contribution subtracted vs coupling strength. Magnification of Fig. 15 near the origin of the attractive branch.

problem in the spin-balanced case, meaning that in principle they do not have problems of accuracy stemming from a variational nodal surface, which affect the DMC method used in both Galea *et al.*'s [22] and Bertaina and Giorgini's [19] papers. However, it includes the mapping from a lattice to a continuous model which strictly holds only in the low-energy regime. Another systematic source of error in all MC simulations is the correction for finite-size effects, which assumes Fermi-liquid theory, and an effective mass equal to the noninteracting case, $M^* = M$. This effect is accounted for by Bertaina and Giorgini [19] with an increased uncertainty. In Shi *et al.*'s [21] paper, the results presented account for the finite-size correction. However, subtracting the finite-size correction brings in additional assumptions: in particular, the difference in energy between the finite-size system and the thermodynamic limit is used, as calculated with BCS theory, which is not exact. In summary, Shi *et al.*'s results are affected by finite-size inaccuracies, which they correct, and the lattice to continuous mapping, while Galea *et al.*'s [22] and Bertaina and Giorgini's [19] results are affected both by variational inaccuracy in the nodal surface and finite-size effects, which are corrected by both Bertaina and Giorgini [19] and Galea *et al.* [22].¹⁷

The repulsive two-dimensional Fermi gas has been studied with fixed-node DMC in Refs. [20,64] for both a hard-disk potential, where a_{2D} is equal to the disk diameter R , and a soft-disk potential where $a_{2D} = 0.5R$. These results are also reported in Fig. 15 for $\alpha > 0$, and are magnified in Fig. 17 for small α . Here, the fixed-node DMC results are systematically slightly higher in energy than the uncertainty band of the EFT prediction. This may be due to slower convergence of the perturbative expansion due to the beyond mean-field contribution alternating sign on the repulsive side. Beyond the inaccuracies in the MC data associated with finite-size effects (which are corrected as in the attractive case) and the nodal surface of the trial wave function, nonuniversal effects may also be important in the repulsive regime. For exam-

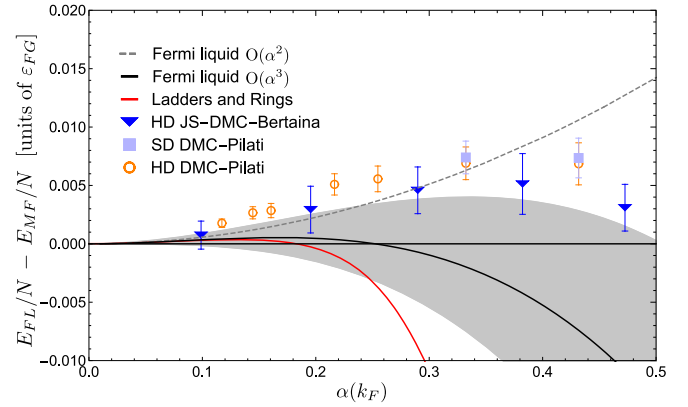


FIG. 17. Energy per particle with mean-field contribution subtracted vs coupling strength. Magnification of Fig. 15 near the origin of the repulsive branch.

ple, in the case of a hard-disk potential, the s -wave effective range is comparable to the a_{2D} parameter $\sqrt{|\sigma_2|} = a_{2D}/\sqrt{2\pi}$ [37]. In Figs. 15 and 17, for $\alpha(k_F) > 0$, the effective range contributions (computed for the hard disk) are included in the Fermi-liquid prediction at $O(\alpha^3)$. This amounts to a 5% effect at $\alpha(k_F) \approx 1$. Note that the fixed-node DMC results for both the soft- and hard-disk potentials are consistent within error bars suggesting that effective range effects are not the major driver of discrepancy between fixed-node DMC and EFT. Both Figs. 16 and 17 highlight that it would be worth pursuing new high-precision MC simulations in the weakly interacting regime, where both finite-size effects and effective range nonuniversality are accurately determined. This is particularly relevant in the repulsive case.

The contact density predictions are compared with MC simulations of the (short-range behavior of the) antiparallel pair distribution function taken from Ref. [20] in Fig. 12.

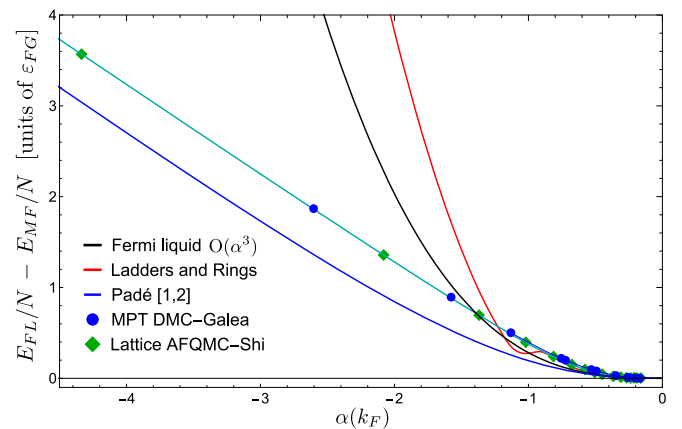


FIG. 18. Energy per particle with mean-field piece subtracted vs coupling strength. MC data are included over all attractive coupling strengths from the BCS region to the BEC region. The data are as described in the text, with LO gap energy subtracted, and connected by the green curve for ease of viewing. The solid black curve is the NNLO Fermi-liquid prediction. The red curve is the complete ladder and ring resummation, and the blue curve is the [1,2] Padé approximant, as discussed in the text.

¹⁷The finite-size correction function implemented by Galea *et al.* is taken from Refs. [65,66].

The gap (molecular) contribution to the contact density is subtracted from the data in the attractive regime. Note that the contact density, unlike the energy per particle shown in Fig. 15, does not have the mean-field contribution subtracted.

Finally, Fig. 18 shows the remarkably smooth and consistent MC data, here with the LO gap energy subtracted (see discussion at the end of Sec. IV C), out to the strong-coupling (BEC) region, where the fermions are expected to form tightly bound pairs which in turn Bose condense. In the three-dimensional case, resumming perturbation theory via Padé approximants and other methods appears to capture strong-coupling trends fairly accurately [67]. While the [2,1] Padé approximant formed from the results of this paper has a low-lying singularity, the [1,2] Padé approximant (shown in Fig. 18) is much closer to the data than the full ladder-ring sum.

X. CONCLUSION

Quantum mechanics on a plane is remarkably rich and yet dramatically distinct from its three-dimensional counterpart, even in the context of the ultracold, weak-coupling results that are considered in this paper. While challenging to realize experimentally, the weakly coupled Fermi gas in two dimensions is tractable analytically and can be simulated to high accuracy using quantum MC techniques. In this paper, the universal interaction has been computed to one order higher than known previously, and the results have been shown to be in excellent agreement with MC simulations for attractive coupling. In addition, various nonuniversal effects of interest have been computed, with the hope that they will inspire specially crafted MC simulations to test their validity. The EFT methodology, with the choice of DR to tame the singular nature of the interaction, proves to be a highly efficient means of systematically improving the description without having to specify the potential.

There are many straightforward generalizations of the results in this paper. The most obvious extension is to compute one order higher in the universal interaction. In three dimen-

sions, the calculation of the energy density has been taken to one higher order [68,69] in the diagrammatic expansion, which is in correspondence with $O(\alpha^4)$ effects in two dimensions. It is noteworthy that at that order there are ≈ 30 Feynman diagrams, most of which are not of ring or ladder type. At this nominal fourth order, resumming perturbation theory via Padé approximants and other methods appears to capture beyond-perturbation-theory strong-coupling trends accurately [67].

Other interesting extensions of the work in this paper in the context of the two-dimensional Fermi gas include the case of dilute Fermi gases with population imbalance [64,70], corrections to the Fermi-liquid quasiparticle parameters [25,26], which have been computed to subleading orders in three dimensions [9], and quantum corrections to the energy density for the p -wave interactions (computed in three dimensions in Ref. [14]). In addition, the role of the p -wave effective range in the many-body system is of current interest both in two and three dimensions [56,58–61,71] and may be profitably studied using the EFT methods of this paper. Also of interest are various corrections and extensions regarding the pairing phenomena. While the p -wave pairing gap was considered in the original papers that addressed superfluidity [28,29], the results were somewhat mysterious due to the highly singular nature of the p -wave interaction. It would be illuminating to address this problem using EFT methods.

ACKNOWLEDGMENTS

We would like to thank E. Berkowitz, David B. Kaplan, Daniel R. Phillips, and Sanjay Reddy for helpful comments and discussions. In addition, we are grateful to A. Gezerlis and S. Gandolfi for making their data available, and for clarifying discussions regarding their work. G.B. acknowledges useful discussions with S. Pilati concerning inaccuracies in MC methods. This work was supported by the U.S. Department of Energy Grant No. DE-FG02-97ER-41014 (UW Nuclear Theory). R.C.F. was also partially supported by the U.S. Department of Energy Grant No. DE-SC0020970 (InQubator for Quantum Simulation).

-
- [1] J. Carlson, S. Gandolfi, and A. Gezerlis, Quantum Monte Carlo approaches to nuclear and atomic physics, *Prog. Theor. Exp. Phys.* **2012**, 01A209 (2012).
 - [2] D. R. Phillips, Building light nuclei from neutrons, protons, and pions, *Czech. J. Phys.* **52**, B49 (2002).
 - [3] D. B. Kaplan, Five lectures on effective field theory, [arXiv:nuc1-th/0510023](https://arxiv.org/abs/nuc1-th/0510023).
 - [4] E. Braaten and H. W. Hammer, Universality in few-body systems with large scattering length, *Phys. Rep.* **428**, 259 (2006).
 - [5] R. J. Furnstahl, J. V. Steele, and N. Tiffessa, Perturbative effective field theory at finite density, *Nucl. Phys. A* **671**, 396 (2000).
 - [6] J. V. Steele, Effective field theory power counting at finite density, [arXiv:nuc1-th/0010066](https://arxiv.org/abs/nuc1-th/0010066).
 - [7] H. W. Hammer and R. J. Furnstahl, Effective field theory for dilute Fermi systems, *Nucl. Phys. A* **678**, 277 (2000).
 - [8] R. J. Furnstahl and H. W. Hammer, Effective field theory for Fermi systems in a large N expansion, *Ann. Phys. (NY)* **302**, 206 (2002).
 - [9] L. Platter, H. W. Hammer, and U. G. Meissner, Quasiparticle properties in effective field theory, *Nucl. Phys. A* **714**, 250 (2003).
 - [10] T. Schäfer, C.-W. Kao, and S. R. Cotanch, Many body methods and effective field theory, *Nucl. Phys. A* **762**, 82 (2005).
 - [11] T. Schäfer, Effective theories of dense and very dense matter, *Lect. Notes Phys.* **852**, 193 (2012).
 - [12] R. J. Furnstahl, H. W. Hammer, and S. J. Puglia, Effective field theory for dilute fermions with pairing, *Ann. Phys. (NY)* **322**, 2703 (2007).
 - [13] N. Kaiser, Resummation of fermionic in-medium Ladder diagrams to all orders, *Nucl. Phys. A* **860**, 41 (2011).

- [14] N. Kaiser, Resummation of in-medium Ladder diagrams: s-wave effective range and p-wave interaction, *Eur. Phys. J. A* **48**, 148 (2012).
- [15] C. Chafin and T. Schaefer, Scale breaking and fluid dynamics in a dilute two-dimensional Fermi gas, *Phys. Rev. A* **88**, 043636 (2013).
- [16] N. Kaiser, Single-particle potential from resummed Ladder diagrams, *Eur. Phys. J. A* **49**, 140 (2013).
- [17] N. Kaiser, Particle-hole ring diagrams for fermions in two dimensions, *Ann. Phys. (NY)* **350**, 549 (2014).
- [18] J. Levinsen and M. M. Parish, Strongly interacting two-dimensional Fermi gases, in *Annual Review of Cold Atoms and Molecules*, edited by K. W. Madison, K. Bongs, L. D. Carr, A. M. Rey, and H. Zhai (World Scientific, Singapore, 2015), Vol. 3, pp. 1–75.
- [19] G. Bertaina and S. Giorgini, BCS-BEC Crossover in a Two-Dimensional Fermi Gas, *Phys. Rev. Lett.* **106**, 110403 (2011).
- [20] G. Bertaina, Two-dimensional short-range interacting attractive and repulsive Fermi gases at zero temperature, *Eur. Phys. J.: Spec. Top.* **217**, 153 (2013).
- [21] H. Shi, S. Chiesa, and S. Zhang, Ground-state properties of strongly interacting Fermi gases in two dimensions, *Phys. Rev. A* **92**, 033603 (2015).
- [22] A. Galea, H. Dawkins, S. Gandolfi, and A. Gezerlis, Diffusion Monte Carlo study of strongly interacting two-dimensional Fermi gases, *Phys. Rev. A* **93**, 023602 (2016).
- [23] A. Galea, T. Zielinski, S. Gandolfi, and A. Gezerlis, Fermions in two dimensions: Scattering and many-body properties, *J. Low Temp. Phys.* **189**, 451 (2017).
- [24] L. Rammelmüller, W. J. Porter, and J. E. Drut, Ground state of the two-dimensional attractive Fermi gas: Essential properties from few- to many-body, *Phys. Rev. A* **93**, 033639 (2016).
- [25] J. R. Engelbrecht, M. Randeria, and L. Zhang, Landau f function for the dilute Fermi gas in two dimensions, *Phys. Rev. B* **45**, 10135 (1992).
- [26] J. R. Engelbrecht and M. Randeria, Low-density repulsive Fermi gas in two dimensions: Bound-pair excitations and Fermi-liquid behavior, *Phys. Rev. B* **45**, 12419 (1992).
- [27] P. Bloom, Two-dimensional Fermi gas, *Phys. Rev. B* **12**, 125 (1975).
- [28] M. Randeria, J.-M. Duan, and L.-Y. Shieh, Bound States, Cooper Pairing, and Bose Condensation in two Dimensions, *Phys. Rev. Lett.* **62**, 981 (1989).
- [29] M. Randeria, J.-M. Duan, and L.-Y. Shieh, Superconductivity in a two-dimensional Fermi gas: Evolution from Cooper pairing to Bose condensation, *Phys. Rev. B* **41**, 327 (1990).
- [30] R. W. Jackiw, Delta function potentials in two-dimensional and three-dimensional quantum mechanics, Report No. MIT-CTP-1937 (World Scientific, Singapore, 1991), pp. 35–53.
- [31] U. van Kolck, Effective field theory of short range forces, *Nucl. Phys. A* **645**, 273 (1999).
- [32] D. B. Kaplan, M. J. Savage, and M. B. Wise, A New expansion for nucleon-nucleon interactions, *Phys. Lett. B* **424**, 390 (1998).
- [33] D. B. Kaplan, M. J. Savage, and M. B. Wise, Two nucleon systems from effective field theory, *Nucl. Phys. B* **534**, 329 (1998).
- [34] E. Braaten and A. Nieto, Renormalization effects in a dilute Bose gas, *Phys. Rev. B* **55**, 8090 (1997).
- [35] S. K. Adhikari, Quantum scattering in two dimensions, *Am. J. Phys.* **54**, 362 (1986).
- [36] S. A. Rakityansky and N. Elander, Analytic structure and power series expansion of the Jost function for the two-dimensional problem, *J. Phys. A: Math. Theor.* **45**, 135209 (2012).
- [37] H. W. Hammer and D. Lee, Causality and the effective range expansion, *Ann. Phys. (NY)* **325**, 2212 (2010).
- [38] S. R. Beane, Ground state energy of the interacting Bose gas in two dimensions: An explicit construction, *Phys. Rev. A* **82**, 063610 (2010).
- [39] S. R. Beane, Effective-range corrections to the ground-state energy of the weakly-interacting Bose gas in two dimensions, *Eur. Phys. J. D* **72**, 55 (2018).
- [40] C. A. Bertulani, H. W. Hammer, and U. Van Kolck, Effective field theory for halo nuclei, *Nucl. Phys. A* **712**, 37 (2002).
- [41] S. R. Beane and R. C. Farrell, Symmetries of the nucleon-nucleon S-matrix and effective field theory expansions, *Few-Body Syst* **63**, 45 (2022).
- [42] J. Polchinski, Effective field theory and the Fermi surface, [arXiv:hep-th/9210046](https://arxiv.org/abs/hep-th/9210046).
- [43] R. Shankar, Renormalization-group approach to interacting fermions, *Rev. Mod. Phys.* **66**, 129 (1994).
- [44] V. M. Loktev, R. M. Quick, and S. G. Sharapov, Phase fluctuations and pseudogap phenomena, *Phys. Rep.* **349**, 1 (2001).
- [45] T. Papenbrock and G. F. Bertsch, Pairing in low density Fermi gases, *Phys. Rev. C* **59**, 2052 (1999).
- [46] M. Marini, F. Pistolesi, and G. Strinati, Evolution from BCS superconductivity to bose condensation: Analytic results for the crossover in three dimensions, *Eur. Phys. J. B* **1**, 151 (1998).
- [47] H. Heiselberg, C. J. Pethick, H. Smith, and L. Viverit, Influence of Induced Interactions on the Superfluid Transition in Dilute Fermi Gases, *Phys. Rev. Lett.* **85**, 2418 (2000).
- [48] L. D. Landau and E. M. Lifshitz, *Statistical Physics*, 3rd ed. translated from the Russian by J. R. Sykes and M. J. Kearsley, Course of Theoretical Physics Vol. 9 (Pergamon Press, New York, 1980), Part 2.
- [49] L. Gor'kov and T. Melik-Barkhudarov, Contribution to the theory of superfluidity in an imperfect Fermi gas, *Zh. Eksp. Teor. Fiz.* **40**, 1452 (1961) [*J. Exp. Theor. Phys.* **13**, 1018 (1961)].
- [50] D. S. Petrov, M. A. Baranov, and G. V. Shlyapnikov, Superfluid transition in quasi-two-dimensional Fermi gases, *Phys. Rev. A* **67**, 031601(R) (2003).
- [51] M. A. Resende, A. L. Mota, R. L. S. Farias, and H. Caldas, Finite temperature phase diagram of quasi-two-dimensional imbalanced Fermi gases beyond mean-field, *Phys. Rev. A* **86**, 033603 (2012).
- [52] A. V. Chubukov, Kohn-Luttinger effect and the instability of a two-dimensional repulsive Fermi liquid at $T = 0$, *Phys. Rev. B* **48**, 1097 (1993).
- [53] S. Tan, Large momentum part of a strongly correlated Fermi gas, *Ann. Phys. (NY)* **323**, 2971 (2008).
- [54] S. Tan, Energetics of a strongly correlated Fermi gas, *Ann. Phys. (NY)* **323**, 2952 (2008).
- [55] F. Werner and Y. Castin, General relations for quantum gases in two and three dimensions: Two-component fermions, *Phys. Rev. A* **86**, 013626 (2012).
- [56] Z. Yu, J. H. Thywissen, and S. Zhang, Universal Relations for a Fermi Gas Close to a p -wave Interaction Resonance, *Phys. Rev. Lett.* **115**, 135304 (2015).
- [57] Y.-C. Zhang and S. Zhang, Strongly interacting p -wave Fermi gas in two dimensions: Universal relations and breathing mode, *Phys. Rev. A* **95**, 023603 (2017).

- [58] M. He and Q. Zhou, p -wave contacts of quantum gases in quasi-one-dimensional and quasi-two-dimensional traps, *Phys. Rev. A* **104**, 043303 (2021).
- [59] M. He and Q. Zhou, s -wave contacts of quantum gases in quasi-one-dimensional and quasi-two-dimensional traps, *Phys. Rev. A* **100**, 012701 (2019).
- [60] S.-L. Zhang, M. He, and Q. Zhou, Contact matrix in dilute quantum systems, *Phys. Rev. A* **95**, 062702 (2017).
- [61] M. He, S. Zhang, H. M. Chan, and Q. Zhou, Concept of a Contact Spectrum and Its Applications in Atomic Quantum Hall States, *Phys. Rev. Lett.* **116**, 045301 (2016).
- [62] A. Fetter, J. Walecka, and B. Banes, *Quantum Theory of Many-Particle Systems*, International Series in Pure and Applied Physics (McGraw-Hill, New York, 1971).
- [63] E. Vitali, H. Shi, M. Qin, and S. Zhang, Visualizing the BEC-BCS crossover in a two-dimensional Fermi gas: Pairing gaps and dynamical response functions from ab initio computations, *Phys. Rev. A* **96**, 061601(R) (2017).
- [64] S. Pilati, G. Orso, and G. Bertaina, Quantum Monte Carlo simulations of two-dimensional repulsive Fermi gases with population imbalance, *Phys. Rev. A* **103**, 063314 (2021).
- [65] H. Shi, Computational studies of strongly correlated quantum matter, Ph.D. thesis, College of William and Mary, 2017.
- [66] A. Galea, Diffusion Monte Carlo study of strongly interacting two-dimensional Fermi gases, Ph.D. thesis, University of Guelph, 2016.
- [67] C. Wellenhofer, D. R. Phillips, and A. Schwenk, From weak to strong: Constrained extrapolation of perturbation series with applications to dilute Fermi systems, *Phys. Rev. Res.* **2**, 043372 (2020).
- [68] C. Wellenhofer, C. Drischler, and A. Schwenk, Dilute Fermi gas at fourth order in effective field theory, *Phys. Lett. B* **802**, 135247 (2020).
- [69] C. Wellenhofer, C. Drischler, and A. Schwenk, Effective field theory for dilute Fermi systems at fourth order, *Phys. Rev. C* **104**, 014003 (2021).
- [70] D. C. W. Foo and G. J. Conduit, Diffusion Monte Carlo study of a spin-imbalanced two-dimensional Fermi gas with attractive interactions, *Phys. Rev. A* **100**, 063602 (2019).
- [71] S. Ding and S. Zhang, Fermi-Liquid Description of a Single-Component Fermi Gas with p -Wave Interactions, *Phys. Rev. Lett.* **123**, 070404 (2019).